Parabolized Navier-Stokes Predictions of Three-Dimensional Hypersonic Flows with Strong Crossflow Effects

Bilal A. Bhutta* and Clark H. Lewis†
VRA, Inc., Blacksburg, Virginia

In this study, a new three-dimensional fully iterative parabolized Navier-Stokes (PNS) scheme has been developed to study perfect-gas or equilibrium-air viscous hypersonic flows around ballistic re-entry configurations at large angles of attack. This three-dimensional PNS scheme is inherently stable in the subsonic as well as the supersonic flow regions and, thus, does not require any sublayer approximation. Furthermore, it uses a generalized PNS formulation to treat perfect-gas and equilibrium-air gas models in a unified manner. A second-order smoothing approach is used to damp the solution oscillations, whereas a pseudo-unsteady approach is used to significantly enhance computational efficiency without compromising solution accuracy. A new fully implicit and crossflow-coupled shock-fitting approach has been used, along with a new predictor-corrector solution scheme to treat large crossflow-separated regions. The flow over a 15-deg sphere-cone configuration at an angle of attack of 20 deg is studied at two different Mach numbers to demonstrate the solution scheme.

Nomenclature

C_p = specific heat at constant pressure
DSHK = linear distance between body and shock
h = static enthalpy of the mixture
J = determinant of the transformation Jacobian
k = mixture thermal conductivity
KMAX = number of grid points in crossflow (ξ_3) direction
LMAX = number of grid points in axis-normal (ξ_2) direction
M = Mach number
m_{nij} = $\xi_{n,x_i}\xi_{n,x_j}$
n = iteration number
p = static pressure
PHI = circumferential angle measured from windward side, ϕ
Pr = Prandtl number
QW = total wall heat-transfer rate
Re = Reynolds number, $(\rho_\infty V_\infty Rn)/\mu_\infty$
RN,Rn = nose radius
T = static temperature
u = x component of velocity
u_j = u, v, and w for $j = 1$, 2, and 3
U_j = contravariant velocities, $u_k\xi_{j,x_k}$
V = total velocity
v,w = y and z components of velocity, respectively
X,x = coordinate along body axis
x_j = x, y, and z for $j = 1$, 2, and 3
α = angle of attack
γ = specific-heat ratio
ε = M_∞/Re_∞
μ = mixture viscosity
ξ_1 = marching or streamwise coordinate
ξ_2 = coordinate measured from the body to the outer bow shock
ξ_3 = coordinate measured from the windward pitch plane to the leeward pitch plane
ρ = mixture density
ϕ = circumferential angle measured from the windward pitch plane to the leeward pitch plane

Superscripts

j = index in ξ_1 direction
n = index for iteration
T = vector transpose

Subscripts

(,) = represents partial derivative
∞ = freestream quantity
i,j = indicial notation representing 1, 2, and 3
k,l = indices in the ξ_3 and ξ_2 directions, respectively
s = shock quantity
w = wall quantity
0 = total condition

Introduction

OVER the past several years, significant advances have been made in the field of computational fluid mechanics (CFD). Several recent advances in computer facilities, their speed and storage capabilities, have made it possible to develop accurate and sophisticated numerical prediction schemes for various high-speed, fluid-flow problems. On the other hand, not only is there a lack of high-speed experimental facilities but also their operating costs have remained very high.

Existing modern methodologies for external-flow prediction over ballistic geometries consist of Navier-Stokes (NS), parabolized Navier-Stokes (PNS), and viscous shock-layer (VSL) schemes. The NS schemes[1-4] are typically very time-consuming and not well suited for various parametric studies required for design and analysis purposes. On the other hand, the existing noniterative PNS schemes[5-8] suffer from instabilities and inaccuracies. Apart from being noniterative, such PNS schemes require a substantial approximation in the way the subsonic sublayer region is treated. Large global conservation-of-mass (as well as momentum and energy) errors are generally associated with these PNS methods, which originate from the basic noniterative solution scheme. The existing VSL schemes[9-11] have as a major limitation that they are parabolic in the crossflow direction and, consequently, cannot march

Presented as Paper 88-2696 at the AIAA Thermophysics, Plasmadynamics, and Lasers Conference, San Antonio, TX, June 27-29, 1988; received July 11, 1988; revision received Feb. 6, 1989.

*Chief Scientist. Member AIAA.
†President. Associate Fellow AIAA.

through crossflow separated regions. This prevents the VSL scheme from accurately predicting the aerodynamic response of complex projectile/missile configurations, which may experience strong crossflow separation, either because of a large-angle-of-attack condition or simply because of the three-dimensional nature of the geometry being considered (such as finned configurations). However, even under these conditions, the flowfield in the nose region is attached, and the VSL schemes represent an accurate and efficient way of generating the nose solutions for starting other (more accurate) afterbody methods that can treat crossflow separation (such as the PNS schemes).

In this paper, we have extended our basic PNS scheme[12-16] to study large-angle-of-attack three-dimensional supersonic/hypersonic flowfields using a general curvilinear coordinate system. However, for simplicity, we considered only axisymmetric geometries in this study. Substantial effort was devoted to the development of a new, fully implicit and crossflow-coupled shock-fitting scheme in which the bow shock shape is predicted as the solution marches down the body. Furthermore, a new predictor-corrector solution scheme was developed and used to treat the strong crossflow coupling effects in and around the crossflow separated region. Two large-angle-of-attack test cases were considered to validate and demonstrate this three-dimensional PNS capability. These test cases deal with the flow over a 15-deg sphere-cone vehicle at an angle of attack of 20 deg. The first test case considered was for Mach 10.6 wind-tunnel conditions and corresponds to one of the test cases studied by Cleary.[17] The second test case involved the flow over the same sphere-cone configuration at a flight Mach number of 20 and for a flight altitude of 45.7 km. Both perfect-gas and equilibrium-air gas models were used to study this test case. The results of these numerical tests are very encouraging and demonstrate quite well the salient features of the new three-dimensional PNS scheme.

Solution Scheme

The coordinate system used for the present three-dimensional PNS scheme is a general curvilinear coordinate system (ξ_1,ξ_2,ξ_3) shown in Fig. 1. The origin of the coordinate system is at the tip of the blunt nose, and the x axis is aligned with the axis of the body. The ξ_1 coordinate is along the body and is also the marching direction. The ξ_2 coordinate is measured from the body to the outer bow shock and lies in an axis-normal plane. The ξ_3 coordinate is measured in the crossflow direction from the windward pitch plane to the leeward pitch plane. In general, it is assumed that the (x,y,z) space is uniquely transformable to the (ξ_1,ξ_2,ξ_3) space through relations of the form

$$\xi_j = \xi_j(x,y,z) \tag{1}$$

The transformation of Eqs. (1) are such that $\Delta\xi_2 = \Delta\xi_3 = 1$ and $\Delta\xi_1 = \Delta x$.

Governing Equations

We choose our unknowns to be the density (ρ), the density-velocity products (ρu, ρv, and ρw), the density-temperature product (ρT), and the pressure (p). Thus, our vector of unknowns is

$$\boldsymbol{q} = [\rho,\rho u,\rho v,\rho w,\rho T,p]^T \tag{2}$$

Following the approach of Peyret and Viviand[18] and Viviand,[19] it can be shown that the full Navier-Stokes equations governing the three-dimensional flow problem can be transformed into the general curvilinear system (ξ_j) and written as

$$(\boldsymbol{e}_j - \varepsilon \boldsymbol{g}_j)_{,\xi_j} = 0 \tag{3}$$

These five equations representing the differential conservation of mass, momentum, and energy are mathematically closed by using the equation of state for the particular gas model used. This equation of state can be written in a general functional form as

$$\gamma_\infty p - Z^* \rho T = 0 \tag{4}$$

In the case of a perfect-gas model, the gas is assumed to be thermally as well as calorically perfect and $Z^* = 1$. In the case of an equilibrium-air gas model, Z^* is a state variable. In the present formulation, Z^* for an equilibrium-air gas model is provided in a tabular form using pressure and temperature as the dependent variable [i.e., $Z^* = Z^*(p,T)$].

Equations (3) are elliptic in ξ_1, ξ_2, and ξ_3 directions. If we neglect the viscous dissipation effects in the ξ_1 direction, we can combine Eqs. (3) and (4) in the following vectorial equation.

$$\boldsymbol{f}_{j,\xi_j} - \varepsilon \boldsymbol{s}_{2,\xi_2} - \varepsilon \boldsymbol{s}_{3,\xi_3} = \boldsymbol{h} \tag{5}$$

Equations (5) represent the PNS equations. The various components of this vectorial equation are defined as

$$\boldsymbol{f}_j = (1/J)\begin{bmatrix} \rho U_j \\ \rho u U_j + \xi_{j,x} p \\ \rho v U_j + \xi_{j,y} p \\ \rho w U_j + \xi_{j,z} p \\ \rho h_o U_j \\ 0 \end{bmatrix}, \qquad \boldsymbol{s}_n = (\mu/J)\begin{bmatrix} 0 \\ m_{nii} u_{,\xi_n} + m_{n1j} u_{j,\xi_n}/3 \\ m_{nii} v_{,\xi_n} + m_{n2j} u_{j,\xi_n}/3 \\ m_{nii} w_{,\xi_n} + m_{n3j} u_{j,\xi_n}/3 \\ m_{nii} T_{,\xi_n} C_p/Pr + m_{nii} u_j u_{j,\xi_n} + m_{nij} u_i u_{j,\xi_n}/3 \\ 0 \end{bmatrix} \tag{6a}$$

where no summation is implied over n, which takes the values of $n = 2$ and 3, respectively. Also,

$$\boldsymbol{h} = [0,0,0,0,0,(\gamma_\infty p - Z^* \rho T)]^T \tag{6b}$$

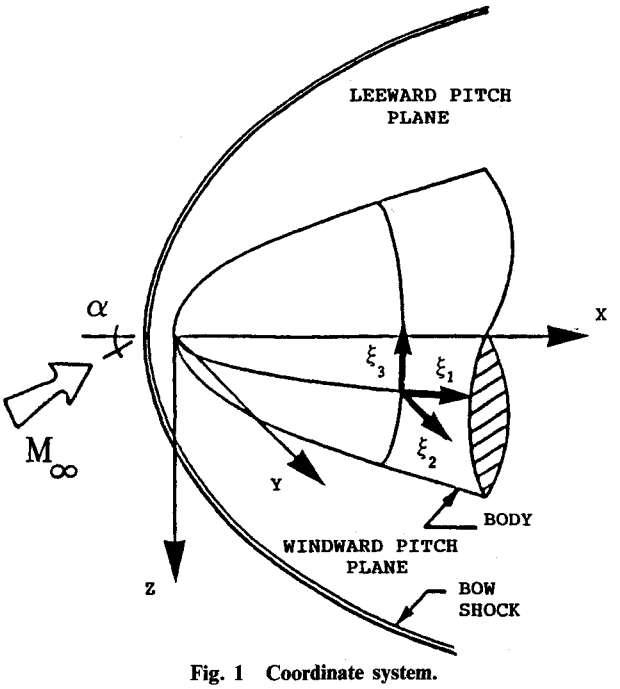

Fig. 1 Coordinate system.

Delta Form of the Governing Equations

In this delta formulation, we solve for the changes in the flowfield variables from one iteration to the next. Let us denote the iteration at which we seek the solution by the superscript $n+1$, and the previous iteration (the solution to which is known) by the superscript n. If we assume that the solution at the $n+1$ iteration is close to the solution at the nth iteration, we can use a first-order Taylor series expansion around the previous iteration to write

$$\begin{aligned} \boldsymbol{f}_j^{j+1,n+1} &\simeq \boldsymbol{f}_j^{j+1,n} + \boldsymbol{A}_j^n \cdot \Delta\boldsymbol{q}^{n+1} \\ \boldsymbol{s}_2^{j+1,n+1} &\simeq \boldsymbol{s}_2^{j+1,n} + \boldsymbol{M}_2^n \cdot \Delta\boldsymbol{q}^{n+1} \\ \boldsymbol{s}_3^{j+1,n+1} &\simeq \boldsymbol{s}_3^{j+1,n} + \boldsymbol{M}_3^n \cdot \Delta\boldsymbol{q}^{n+1} \\ \boldsymbol{h}^{j+1,n+1} &\simeq \boldsymbol{h}^{j+1,n} + \boldsymbol{A}_0^n \cdot \Delta\boldsymbol{q}^{n+1} \end{aligned} \tag{7}$$

where

$$\Delta\boldsymbol{q}^{n+1} = \boldsymbol{q}^{j+1,n+1} - \boldsymbol{q}^{j+1,n} \tag{8}$$

The full PNS equations, given by Eqs. (5), are elliptic in the ξ_2 and ξ_3 directions so that, for second-order accuracy, we use central-differenced approximations for all ξ_2 and ξ_3 derivatives. However, the use of central-differenced schemes is typically associated with solution oscillations.[5-8,12-16] In order to damp these solution oscillations, it is necessary to add some additional higher-order diffusion terms to Eqs. (5). In our earlier work,[12-16] we have developed a second-order-accurate smoothing approach that is accurate and simple to use. In the present study we extend this basic approach to write Eqs. (5) as

$$\begin{aligned} &\boldsymbol{f}_{j,\xi_j}^{j+1,n+1} - \varepsilon(\boldsymbol{s}_{2,\xi_2}^{j+1,n+1} + \boldsymbol{s}_{3,\xi_3}^{j+1,n+1}) - \boldsymbol{h}^{j+1,n+1} \\ &\quad = \boldsymbol{\pi}_1(\boldsymbol{q})\Delta\xi_2)^2 + \boldsymbol{\pi}_2(\boldsymbol{q})(\Delta\xi_3)^2 \end{aligned} \tag{9}$$

where the forms of the vectors $\boldsymbol{\pi}_1$ and $\boldsymbol{\pi}_2$ are chosen such that (to second-order accuracy) we can rewrite Eqs. (5) in terms of an intermediate solution $\boldsymbol{\chi}_1$ as

$$[\boldsymbol{f}_j(\boldsymbol{\chi}_1)]_{,\xi_j} - \varepsilon[\boldsymbol{s}_2(\boldsymbol{\chi}_1)]_{,\xi_2} - \varepsilon[\boldsymbol{s}_3(\boldsymbol{\chi}_1)]_{,\xi_3} - \boldsymbol{h}(\boldsymbol{\chi}_1) = 0 \tag{10}$$

The actual solution at the $j+1$ step ($\boldsymbol{q}^{n+1}$) is related to this intermediate solution by

$$\bar{\boldsymbol{\chi}} = \boldsymbol{\chi}_1 + \boldsymbol{\chi}_{1,\xi_3\xi_3}\,\Delta\xi_3^2/4 \tag{11a}$$

$$\boldsymbol{q}^{n+1} = \bar{\boldsymbol{\chi}} + \bar{\boldsymbol{\chi}}_{,\xi_2\xi_2}\,\Delta\xi_2^2/4 \tag{11b}$$

In the current study, we have further taken the approach of including the crossflow smoothing represented by Eqs. (11a) in the solution of Eqs. (10), so that we directly solve for $\bar{\boldsymbol{\chi}}$ rather than $\boldsymbol{\chi}_1$. It can be shown that by using Eqs. (9-11), we can also write Eqs. (5) to second-order accuracy as

$$\begin{aligned} &[\boldsymbol{f}_j(\bar{\boldsymbol{\chi}})]_{,\xi_j} - \varepsilon[\boldsymbol{s}_2(\bar{\boldsymbol{\chi}})]_{,\xi_2} - \varepsilon[\boldsymbol{s}_3(\bar{\boldsymbol{\chi}})]_{,\xi_3} - \boldsymbol{h}(\bar{\boldsymbol{\chi}}) \\ &\quad = (\boldsymbol{A}_1/\Delta\xi_1 - \boldsymbol{A}_0)\cdot\bar{\boldsymbol{\chi}}_{,\xi_3\xi_3}\,\Delta\xi_3^2/4 = \boldsymbol{\pi}\,\Delta\xi_3^2 \end{aligned} \tag{12}$$

The right-hand side of Eqs. (12) gives the appropriate form of the implicit and explicit smoothing operator to be added to the implicit (left-hand) side and the explicit (right-hand) side of Eqs. (5). As far as the smoothing effects in the ξ_2 direction are concerned [Eqs. (11b)], they are further modified to limit them to the pressure fluid only. In this manner, the velocity and temperature gradients near the wall remain unaffected and, consequently, there is not degradation of the wall heat-transfer and skin-friction predictions.

Thus, the final form of the system of equations to be solved becomes

$$\begin{aligned} &(\boldsymbol{A}_1/\Delta\xi_1 - \boldsymbol{A}_0)^n\cdot(\Delta\bar{\boldsymbol{\chi}} - \Delta\bar{\boldsymbol{\chi}}_{,\xi_3\xi_3}\Delta\xi_3^2/4)^{n+1} \\ &\quad + [(\boldsymbol{A}_2 - \varepsilon\boldsymbol{M}_2)^n\cdot\Delta\bar{\boldsymbol{\chi}}^{n+1}]_{,\xi_2} + [(\boldsymbol{A}_3 - \varepsilon\boldsymbol{M}_3)^n\cdot\Delta\bar{\boldsymbol{\chi}}^{n+1}]_{,\xi_3} \\ &\quad = -[\boldsymbol{f}_{j,\xi_j} - \varepsilon(\boldsymbol{s}_{2,\xi_2} + \boldsymbol{s}_{3,\xi_3}) - \boldsymbol{h} - \boldsymbol{\pi}\,\Delta\xi_3^2]^{j+1,n} \end{aligned} \tag{13a}$$

where

$$\boldsymbol{q}^{n+1} = \bar{\boldsymbol{\chi}} + [0,0,0,0,0,(\bar{\chi}_{6,\xi_2\xi_2}\,\Delta\xi_2^2/4)]^T \tag{13b}$$

and $\bar{\chi}_6$ is the sixth element of the $\bar{\boldsymbol{\chi}}$.

For the perfect-gas model, the mixture viscosity was obtained using the Sutherland formula,[20] and the specific-heat ratio was assumed to be a constant (1.4 for air). The mixture Prandtl number was also assumed fixed (0.72 for air), and the mixture thermal conductivity was obtained from the definition of mixture Prandtl number. For equilibrium-air flows, the mixture thermodynamic and transport properties were provided in the form of a table, using pressure and temperature as the dependent variables. The mixture enthalpy $[h(p,T)]$ and mixture density $[\rho(p,T)]$ data were based on the tabular data of Miner et al.,[21] and the viscosity and thermal conductivity data were based on the data developed by Peng and Pindroh.[22] The Prandtl number data were developed using these viscosity and thermal conductivity data, and the mixture specific-heat data obtained by numerically differentiating the enthalpy data of Miner et al.[21] The equilibrium-air thermodynamic and transport property table thus generated covered the temperature range of 10-15,000 K and the pressure range 2.5331×10^2-1.6059×10^6 N/m^2. It should be noted that these ranges adequately cover most of the flight regime in which the equilibrium-air effects may be important.

Pseudounsteady Solution Algorithm

The terms on the right-hand side of Eqs. (13a) are actually the governing differential equations written at the nth iteration level and go to zero in the limit of convergence. Under these conditions, the exact form of the left-hand implicit terms is of no great consequence except that it affects the convergence path of the solution.[12-16] With this idea in mind, we do not update the Jacobian matrices beyond the first iteration. With this pseudounsteady approach, the converged limit of the final solution is the same as the converged limit of Eqs. (5) and (13a). However, with the present pseudounsteady approach, the time for each iteration after the first iteration ($n=2,3,\ldots$) is only 15-20% of the time taken by the first iteration.

Experience shows that when fine grids or a poor initial guess are used, the solution convergence can be greatly enhanced by using an underrelaxation approach. In order to underrelax the solution, when updating the solution vector from the n to the $n+1$ iteration, we assume that

$$\boldsymbol{\chi}^{n+1} = \omega\bar{\boldsymbol{\chi}}^{n+1} + (1-\omega)\boldsymbol{\chi}^n \tag{14}$$

where $\boldsymbol{\chi}$ is the underrelaxed solution and $\bar{\boldsymbol{\chi}}$ the unrelaxed solution to Eqs. (13a). Thus, in terms of the underrelaxed solution ($\boldsymbol{\chi}$), we can write Eqs. (13a) as

$$\begin{aligned} &(\boldsymbol{A}_1/\Delta\xi_1 - \boldsymbol{A}_0)^n\cdot(\Delta\boldsymbol{\chi} - \Delta\boldsymbol{\chi}_{,\xi_3\xi_3}\,\Delta\xi_3^2/4)^{n+1} \\ &\quad + [(\boldsymbol{A}_2 - \varepsilon\boldsymbol{M}_2)^n\cdot\Delta\boldsymbol{\chi}^{n+1}]_{,\xi_2} \\ &\quad + [(\boldsymbol{A}_3 - \varepsilon\boldsymbol{M}_3)^n\cdot\Delta\boldsymbol{\chi}^{n+1}]_{,\xi_3} \\ &\quad = -\omega[\boldsymbol{f}_{j,\xi_j} - \varepsilon(\boldsymbol{s}_{2,\xi_2} + \boldsymbol{s}_{3,\xi_3}) - \boldsymbol{h} - \boldsymbol{\pi}\,\Delta\xi_3^2]^{j+1,n} = \boldsymbol{g}^n \end{aligned} \tag{15a}$$

where $0 \le \omega \le 1$. The final smoothed solution is related to this underrelaxed solution by

$$q^{n+1} = \chi + [0,0,0,0,0,(\chi_{6,\xi_2\xi_2}\,\Delta\xi_2^2/4)]^T \qquad (15b)$$

where χ_6 is the sixth element of χ. An advantage of using underrelaxation of the solution in this particular form is that the underrelaxation factor (ω) can be varied from one iteration to the next without changing the form of the matrices on the implicit left-hand side of the equations. Consequently, the use of underrelaxation in this manner does not disrupt our present pseudounsteady formulation, in which the coefficient matrices are not changed after the first iteration. Figure 2 shows some typical variations of the L_2 norm of the residuals for $\omega = 0.25$, 0.5, and 0.75, respectively. As can be seen from this figure, the $\omega = 0.75$ results show some convergence difficulties, whereas results with $\omega = 0.5$ and $\omega = 0.25$ show significantly better convergence characteristics. Typically, we start the iterations with a smaller value of ω (0.1 or less) and gradually increase it during the iterations to a higher value. Experience shows that, for almost all cases, ω can be quickly increased to 0.5, while a fast and monotonic solution convergence is maintained.

Predictor-Corrector Solution Scheme

Under large-angle-of-attack conditions, strong crossflow separated regions may develop on the leeward side. Under these conditions, solution coupling in the crossflow direction is very important. If these coupling effects are not properly considered during the iterative solution, they can cause severe convergence difficulties. In order to address the problem of crossflow coupling, we have developed a new predictor-corrector approach. This predictor-corrector scheme is divided into three different parts; namely, 1) the predictor step, 2) the shock solution, and 3) the corrector step.

Using a two-point streamwise differencing and central-differenced approximations in the ξ_2 and ξ_3 directions, the final differenced equations corresponding to Eqs. (15a) can be written in the following block-pentadiagonal form.

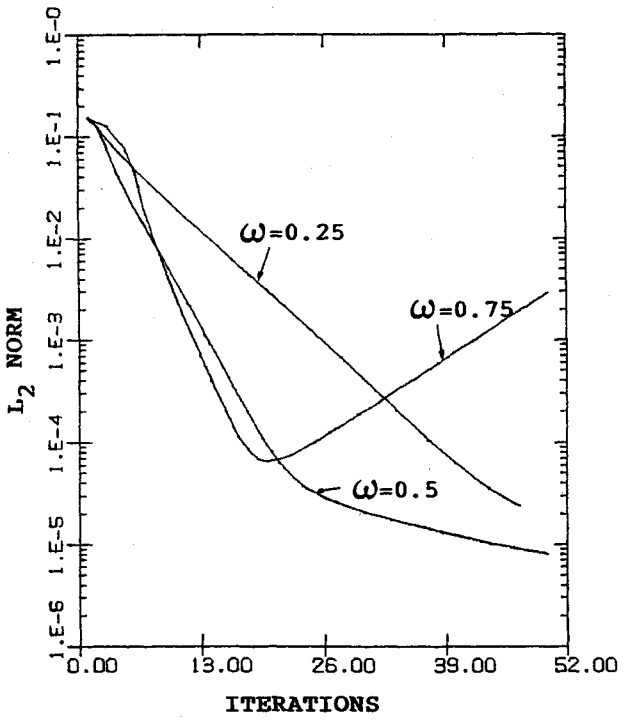

Fig. 2 Effects of underrelaxation on solution convergence.

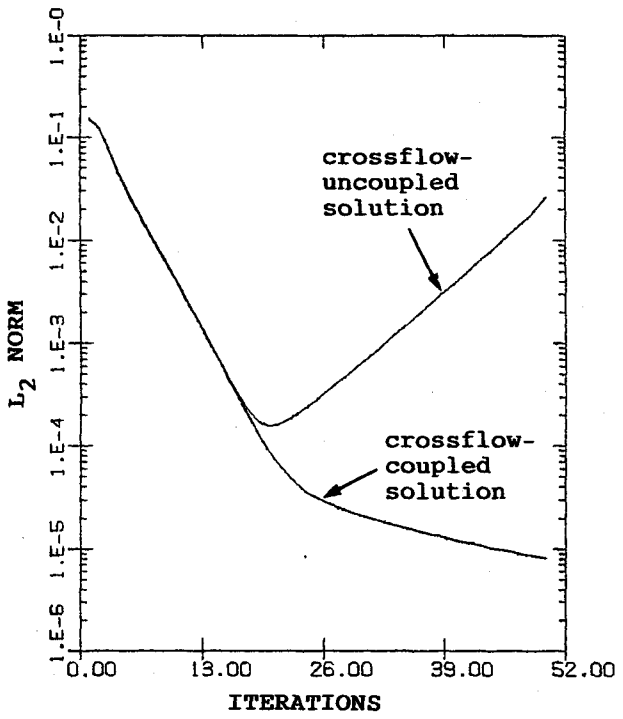

Fig. 3 Effects of crossflow coupling on solution convergence.

$$[A \cdot \Delta\chi_{k,l-1}] + [B \cdot \Delta\chi_{k,l}] + [C \cdot \Delta\chi_{k,l+1}] + [D \cdot \Delta\chi_{k-1,l}] + [E \cdot \Delta\chi_{k+1,l}] = g^n \qquad (16)$$

Predictor Step

In the predictor step, we first neglect the implicit crossflow coupling effects in favor of the body-normal coupling effects. With this assumption, the governing equations for the predictor step become

$$[A \cdot \Delta\chi^*_{k,l-1}] + [B \cdot \Delta\chi^*_{k,l}] + [C \cdot \Delta\chi^*_{k,l+1}] = g^n \qquad (17a)$$

These equations are inverted from the body to the shock to develop a recursive relationship between the solution at each successive grid point in the body-normal direction. These recursive relations have the form

$$\Delta\chi^*_{k,l} = -R_{k,l} \cdot \Delta\chi^*_{k,l+1} + r^n_{k,l} \qquad (17b)$$

where $k = 1, \ldots$ KMAX, $l = 1, \ldots$ LMAX $- 1$, and (χ^*) is the result of the predictor step.

Crossflow-Coupled Shock Solution

Using the recursive relation from the predictor step at the $l =$ (LMAX-1) location, the Rankine-Hugoniot shock-crossing equations are solved to obtain the solution at the shock. This shock solution, along with the solution of the predictor step, is then used to solve the corrector step.

Corrector Step

The solution in the corrector step uses the recursive relations from the predictor step to eliminate the $(k,l-1)$ contributions in the difference molecule. Then, assuming that the solution at the $(k,l+1)$ point can be adequately approximated from the predictor step, we can reduce the Eqs. (16) to only a coupled system of equations in the crossflow direction. This crossflow corrector solution can be written as

$$D \cdot \Delta\chi_{k-1,l} + (B - A \cdot R_{k,l-1}) \cdot \Delta\chi_{k,l} + E \cdot \Delta\chi_{k+1,l} = (g^n - A \cdot r^n_{k,l-1}) - C \cdot \Delta\chi^*_{k,l} \qquad (18)$$

where χ^* is the predicted solution and χ the final corrected solution. Equations (18) can now be solved using plane-of-symmetry boundary conditions applied in the windward and leeward pitch planes, and the corresponding final smoothed solution is obtained using Eqs. (15b).

The effects of crossflow coupling of the solution can be seen in Fig. 3. This figure shows the typical changes in the L_2 norm with increasing number of iterations for 1) a crossflow-coupled solution (using the predictor-corrector scheme) and 2) a crossflow-uncoupled solution (using only the predictor step). Our earlier experience with coarse crossflow grids and with small angles of attack was that, under these conditions, the aforementioned crossflow-uncoupled solution scheme typically showed fast and monotonically convergent characteristics.[14,16] However, Fig. 3 shows that, under large-angle-of-attack conditions and with fine crossflow grids, this uncoupled solution scheme eventually diverges whereas, for the same conditions, the corresponding predictor-corrector solution scheme remains monotonically convergent.

Boundary Conditions

The initial conditions to start the perfect-gas and equilibrium-air PNS solutions were obtained from a VSL blunt-body solution scheme for perfect-gas and equilibrium-air flows.[9,11,23] The quality of such VSL solutions has been discussed in great detail by Thompson et al.[11] and Bhutta et al.[24] The VSL blunt-body solution is interpolated to obtain the starting solution at the initial data plane (IDP) for the three-dimensional PNS afterbody solution. We typically choose the starting location to be approximately 2–3 nose radii downstream of the nose stagnation-point location.

In the present study, the boundary conditions at the windward and leeward pitch planes consist of second-order-accurate reflective or symmetric boundary conditions.[5,6] The boundary conditions at the outer bow shock are, however, much more complicated and involve a fully implicit and crossflow-coupled shock-fitting approach. The boundary conditions at the wall consist of six independent relations representing the nature of the gas mixture and the physical conditions at the wall. These conditions are 1) the equation of state of the gas ($\gamma_\infty p - Z^*\rho T = 0$), 2) no-slip condition for u velocity component ($\rho u = 0$), 3) no-slip condition for v velocity component ($\rho v = 0$), 4) no-slip condition for w velocity component ($\rho w = 0$), 5) a specified wall temperature distribution [$(\rho T) = \rho T_w$], and 6) zero pressure gradient in the ξ_2 direction ($p_{,\xi_2} = 0$).

Implicit Crossflow-Coupled Shock-Fitting

In this approach, the bow shock location is iteratively predicted as the solution marches down the body. The important features of this fully implicit shock-fitting approach are:

1) The bow shock shape location is predicted along with the flowfield solution and does not have to be specified a priori.

2) Unlike earlier noniterative shock-propagation approaches,[5,6,25] the present shock-fitting scheme is fully iterative and treats the various gas models accurately and in a unified manner.

3) Unlike earlier noniterative shock-propagation approaches,[5,6,25] the present approach does not assume that the flowfield behind the shock is inviscid. This can be quite important when strong flowfield gradients exist behind the shock, as may be the case in the nose-dominated region and in regions where the bow shock starts to interact with the embedded shock waves (or compression waves) originating from the body.

4) Unlike the iterative shock-fitting approaches of Helliwell et al.[26] and Lubard and Helliwell,[27] not only is the present shock-fitting approach for a general curvilinear coordinate system, but it also does not increase the matrix size of the block-matrix solution between the body and the shock.

5) The present shock-fitting scheme does not neglect the crossflow coupling effects at the shock. This results in accurate and smooth shock shapes even when there are strong crossflow variations of the conditions behind the shock. This can be especially important when dealing with complex three-dimensional configurations, where the nature of the body can interact with the bow shock and substantially distort it. Similar strong crossflow variations may also occur on simple configurations pitched at large angles of attack.

In developing the present bow shock-fitting scheme, we assume that, from one iteration to the next, the shock points move along the ξ_2 grid line. With this assumption, the final solution has only one additional unknown at the shock that completely defines the spatial movement of the shock point. This smaller number of unknowns is very important for a faster iterative solution and faster convergence characteristics of the overall implicit shock-prediction scheme. This simplification represents only a certain constraint on the direction in which the shock point moves and has no effect on the accuracy of the shock-crossing equations. Thus, the corresponding movement of the shock-point coordinates from one iteration to the next can be written as

$$(x_j)_s^{n+1} \simeq (x_j)_s^n + (x_{j,\xi_2})_s^n (\Delta)_s^{n+1} \tag{19}$$

where Δ_s denotes the amount by which the shock moves in the ξ_2 direction between iterations n and $n+1$.

After defining the appropriate shock-normal and shock-tangent velocity components at the shock, we can write the five Rankine-Hugoniot shock-crossing equations representing the conservation of mass, momentum, and energy across the shock, in terms of the following seven unknowns

$$\boldsymbol{q}_s = [\rho, \rho u, \rho v, \rho w, \rho T, p, \Delta]_s^T \tag{20}$$

Thus, we need two more equations to close the system of equations at the shock. One of these additional equations is the equation of state of the gas, and the other equation is provided by applying the differential continuity of mass equation behind the shock. As we see, no approximation other than the assumption of a Rankine-Hugoniot shock has been made. These equations are equally valid whether the conditions behind the shock are viscous- or inviscid-dominated or whether substantial flowfield gradients exist behind the shock.

If subscripts n, t, and s denote the velocity components in the shock-normal and shock-tangent directions, the seven governing equations at the shock can be written as

$$h + V^2/2 - (h_0)_\infty = 0 \tag{21a}$$

$$\rho V_n - \rho_\infty (V_n)_\infty = 0 \tag{21b}$$

$$\rho[V_t - (V_t)_\infty] = 0 \tag{21c}$$

$$\rho[V_s - (V_s)_\infty] = 0 \tag{21d}$$

$$p - p_\infty + \rho(V_n)^2 - \rho_\infty (V_n)_\infty^2 = 0 \tag{21e}$$

along with the equation of state written in the functional form,

$$\gamma_\infty p - Z^*\rho T = 0 \tag{21f}$$

and the differential continuity equation written as

$$[\xi_{i,x_j} \rho u_j / J]_{,\xi_i} = 0 \tag{21g}$$

The dependence of all of the quantities appearing in Eqs. (21a–g) on the seven unknowns at the shock point ($\boldsymbol{q}_s$) can now be completely described. Furthermore, these equations can be linearized around the previous iteration. Using central-differenced approximations for ξ_3 derivatives and backward-

differenced approximations for ξ_1 and ξ_2 derivatives, we can rewrite these equations in the form

$$(A_s)_k^n \cdot (\Delta q_s)_{k-1}^{n+1} + (B_s^*)_k^n \cdot (\Delta q_s)_k^{n+1} + (C_s)_k^n \cdot (\Delta q_s)_{k+1}^{n+1} + \begin{bmatrix} (D_s)_k^n & 0 \\ 0 & 0 \end{bmatrix} \cdot \begin{bmatrix} \Delta\chi_{k,\mathrm{LMAX}-1}^{n+1} \\ 0 \end{bmatrix} = (g_s^*)_k^n \quad (22)$$

As can be seen from Eqs. (22), the solution of the equations at the shock are coupled to the inner flowfield solution through $\Delta\chi_{k,\mathrm{LMAX}-1}^{n+1}$. Using the results of the predictor step [Eqs. (17a) and (17b)], the inner flowfield solution can now be related to the shock-point solution vector Δq_s^{n+1} through relations of the form

$$\Delta\chi_{k,\mathrm{LMAX}-1}^{n+1} = -[R_{k,\mathrm{LMAX}-1}0] \cdot (\Delta q_s)_k^{n+1} + r_{k,\mathrm{LMAX}-1}^n \quad (23)$$

After substituting Eqs. (23) into Eqs. (22), we can reduce Eqs. (22) to the form

$$A_k^n \cdot (\Delta q_s)_{k-1}^{n+1} + B_k^n \cdot (\Delta q_s)_k^{n+1} + C_k^n \cdot (\Delta q_s)_{k+1}^{n+1} = g_k^n \quad (24)$$

Equations (24) are now solved using appropriate reflective and symmetric boundary conditions in the leeward and windward pitch planes of symmetry. This solution gives simultaneously the Δq_s^{n+1} vectors at each shock point ($k = 1,2,3,...,\mathrm{KMAX}$).

Important Features of the Present Three-Dimensional PNS Scheme

The new three-dimensional PNS scheme being presented offers several advantages and improvements over the existing iterative as well as noniterative PNS schemes. Some of the major features can be briefly summarized as follows:

1) Unlike the existing iterative[26,27] as well as noniterative[5–8] PNS schemes, an eigenvalue analysis of the present PNS formulation shows unconditionally real eigenvalues in the subsonic as well as the supersonic flow regions.[14,15] Consequently, in the absence of streamwise separation, the present PNS formulation is unconditionally timelike and does not require the use of any sublayer approximation.

2) Because the present PNS formulation involves an inherently stable, embedded subsonic region, it can be successfully used under high-altitude and low-Reynolds-number conditions, where the embedded subsonic region is quite thick and can include as much as 50% of the computational grid.[13–15] On the other hand, most of the existing iterative as well as noniterative PNS schemes typically suffer from a breakdown of the sublayer approximation under these high-altitude and low-Reynolds-number conditions.[13–15]

3) Unlike the most commonly used noniterative PNS schemes,[5–8] the present three-dimensional PNS approach does not involve any arbitrary external parameters for controlling the amount of numerical smoothing included in the governing equations. The form and magnitude of the numerical smoothing operators used in the present approach have a fixed and mathematically dictated nature that depends only on the order of the numerical accuracy used. Although the present approach uses a second-order-accurate smoothing formulation, if necessary, a similar fourth-order-accurate formulation can also be derived. The numerical accuracy of the present smoothing approach is clearly reflected in the predicted results, which show almost no dependence on the axis-normal grid refinement.[12–16]

4) The present approach successfully solves a fully conservative set of governing equations using a fully iterative solution scheme and with no sublayer approximation. Moreover, the higher-order numerical dissipation effects are kept at a minimum required level. Consequently, the governing differenced equations are solved in a "clean" form to whatever numerical accuracy is required. Global conservation checks show that, typically, a similar order of accuracy is also reflected in the satisfaction of global conservation of mass, momentum, and energy. All existing iterative or noniterative PNS schemes lack this capability as a result of various deficiencies in the numerical solution schemes used. For example, the existing iterative PNS schemes[26,27] solve the nonconservative form of the equations, whereas the existing noniterative PNS schemes have no direct control or check on the accuracy of the numerical solution. In both cases, further inaccuracies are also introduced through the use of sublayer approximations and excessive numerical smoothing.

5) The present three-dimensional PNS approach also involves the use of a new fully implicit shock-fitting algorithm along with a new predictor-corrector solution scheme. These schemes represent substantially enhanced capabilities over existing schemes used for similar purposes. For example, compared to the present implicit shock-fitting scheme, the existing schemes are less accurate, numerically less stable, and considerably more restrictive in terms of their applicability. Most important, unlike any other shock-fitting scheme, the present approach can accurately treat various gas models in a unified manner. As far as the new predictor-corrector solution scheme is concerned, the results clearly show that it has stability and convergence characteristics greatly superior to the conventionally used approximate factorization approach, whereas the amount of computational effort involved is the same. This enhanced solution capability of the predictor-corrector scheme is even more evident for complicated flowfield conditions, where the crossflow and axis-normal solution coupling effects are important. For the corresponding approximate factorization approach, these coupling effects cause large factorization errors.

6) One of the important features of the present three-dimensional PNS scheme, which is of significant practical interest, is the overall computational efficiency it offers. This numerical formulation uses the iterative aspects of the solution scheme in such a way that the required computational time is substantially reduced; however, the final solution accuracy is not compromised. Furthermore, the enhanced solution stability and accuracy permits the use of much larger marching steps than the corresponding noniterative PNS schemes. Consequently, with the present approach, the flowfield predictions are not only significantly more accurate than the corresponding noniterative schemes, but the final computing times for typical three-dimensional calculations are also shorter. For example, for comparison purposes, we studied the Mach 20 perfect-gas flow over a 5-deg sphere-cone vehicle at an altitude of 30.4 km and an angle of attack of 5 deg. The particular sphere-cone geometry used was 800 Rn long and had a nose radius of 0.00254 m. The flow was fully laminar, and the wall temperature was fixed at 1111.1 K. With our three-dimensional PNS scheme, we could accurately perform this calculation using 50 points between the body and the shock and 9 crossflow planes. This calculation took less than 5 min on an IBM3090 (model 200VF) machine. The corresponding calculations with the AFWAL PNS code[28] required very small axial steps and finer crossflow as well as axis-normal grids. With 19 crossflow planes and 90 points between the body and the shock, the AFWAL PNS calculations took slightly more than 30 min on the Cray-2 machine (which converts to nearly 1 h on the IBM3090). It is worth noting that, even with the 19 crossflow planes, the AFWAL PNS predictions were not as accurate as the predictions of our three-dimensional PNS scheme using only 9 crossflow planes. Preliminary results showed that when the number of crossflow planes in the AFWAL PNS calculations was increased to 45, the predicted results agreed better with our three-dimensional predictions. It is estimated that for the full body length, such a 45-plane solution with the AFWAL PNS code would take nearly 2 h on the Cray-2 machine.

Results and Discussion

In order to test the accuracy and efficiency of the proposed three-dimensional PNS scheme, we studied the flow over a

Table 1 Freestream conditions

Quantity	Case 1	Case 2
Mach number	10.600	20.000
Reynolds number	1.318E + 5	1.952E + 4
Pressure, kN/m^2	1.321E − 1	1.362E − 1
Density, kg/m^3	9.710E − 3	1.792E − 3
Temperature, K	4.734E + 1	2.645E + 2
Velocity, m/s	1.462E + 3	6.522E + 3
Wall temperature, K	3.000E + 2	1.111E + 3
Angle of attack, deg	20.000	20.000

15-deg sphere-cone configuration at an angle of attack of 20 deg at two different Mach numbers. The freestream conditions for this case are given in Table 1. This sphere-cone geometry consists of a 0.02794-m nose radius and has a body length of 17.5 nose radii.

The first test case (case 1) is for a Mach 10.6 wind-tunnel condition. This test case has also been studied by Cleary[17] in the NASA Ames hypersonic wind tunnel. Cases 1a–1c represent the three different computational grids uses to predict the flowfield using a perfect-gas model. Case 1a uses 31 circumferential planes and 50 points between the body and the shock. Case 1b uses 25, and case 1c 17, circumferential planes. The grid size at the wall for these case 1 grids was 0.01% of the local shock-standoff distance. The second test case (case 2) is for a Mach number of 20 and for flight conditions corresponding to an altitude of 45.72 km. Case 2a represents the solution using a perfect-gas model, whereas case 2b represents the corresponding solution using an equilibrium-air gas model. Like the case 1a grid, case 2a and case 2b grids use 31 circumferential planes and 50 points between the body and the shock. The grid distribution in the ξ_2 direction was the same as the one used for case 1. Case 2c calculations use 30 points between the body and the shock and were performed to study the effects of the axis-normal grid refinement on the predictions of the wall-measurable quantities.

Comparison with Experimental Data

As mentioned before, the Mach 10.6 test case (case 1) was also one of the cases studied by Cleary[17] in the NASA Ames hypersonic wind tunnel. This particular test case was considered because the experimental data showed laminar flow over most of the flowfield, except for some transition effects on the lee side. Thus, in this case, most of the flowfield can be accurately modeled using a laminar perfect-gas model. The crossflow velocity vectors presented in Fig. 4 clearly show the crossflow separated region on the leeward side. The crossflow pressure contours for this case indicate that the wall pressure reaches a minimum just before the crossflow separation and then increase slowly toward the leeward pitch plane. The density contours show rapid expansion of the flowfield as we move from the windward to the leeward pitch plane, and the corresponding temperature contours indicate a rapid thickening of the viscous layer in the region of crossflow separation.

The axial and crossflow distributions of wall heat-transfer rate are plotted in Figs. 5 and 6. The corresponding experi-

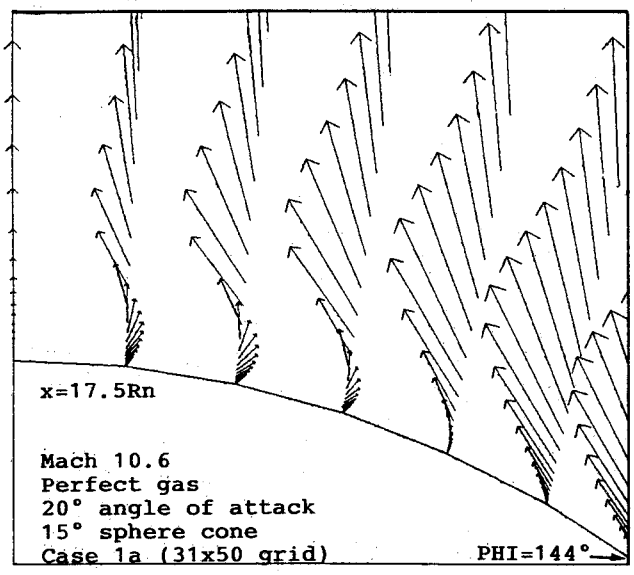

Fig. 4 Lee side crossflow velocity vectors for case 1a.

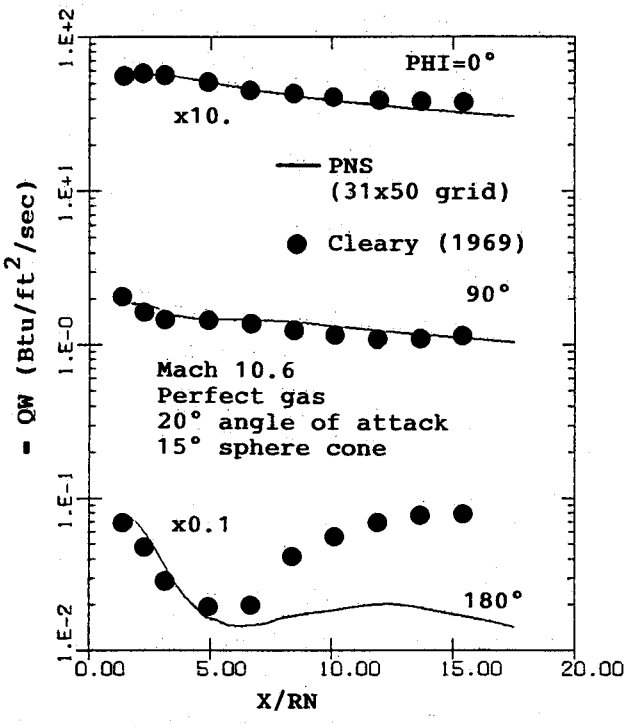

Fig. 5 Axial distribution of wall heat-transfer rate for case 1a.

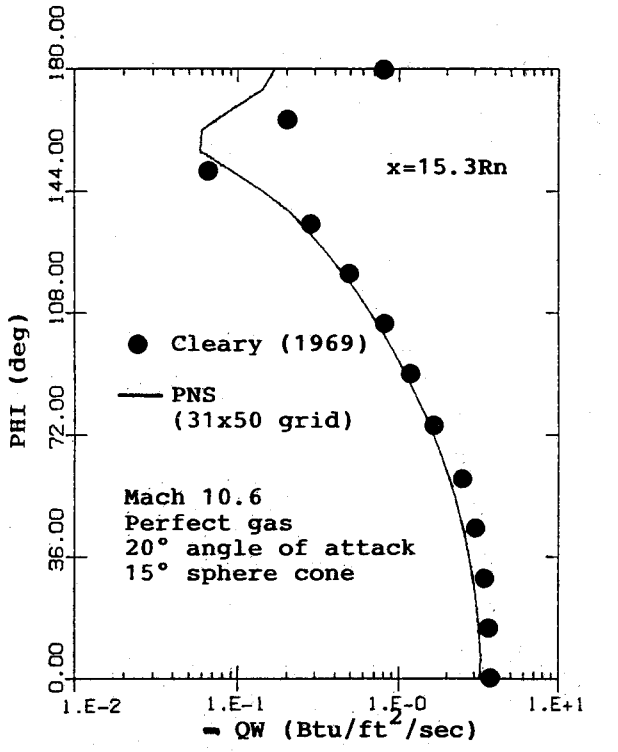

Fig. 6 Crossflow distribution of wall heat-transfer rate for case 1a.

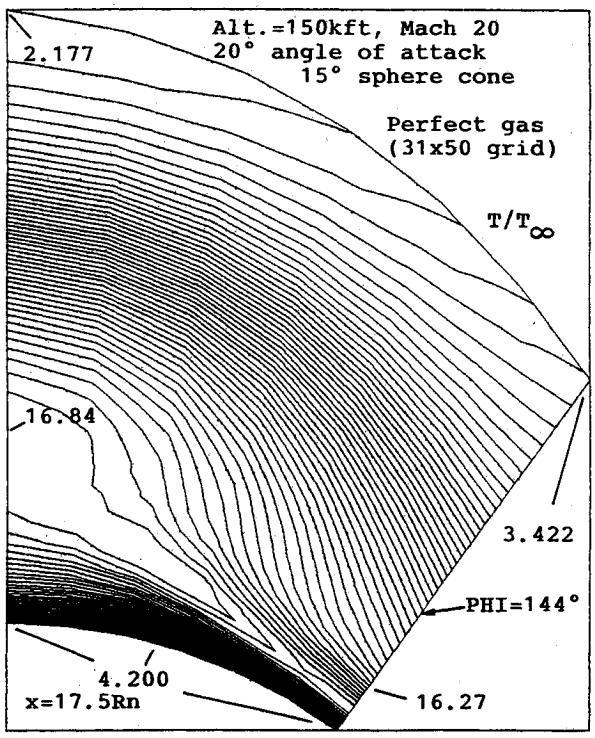

Fig. 7a Details of the lee side temperature contours for case 2a.

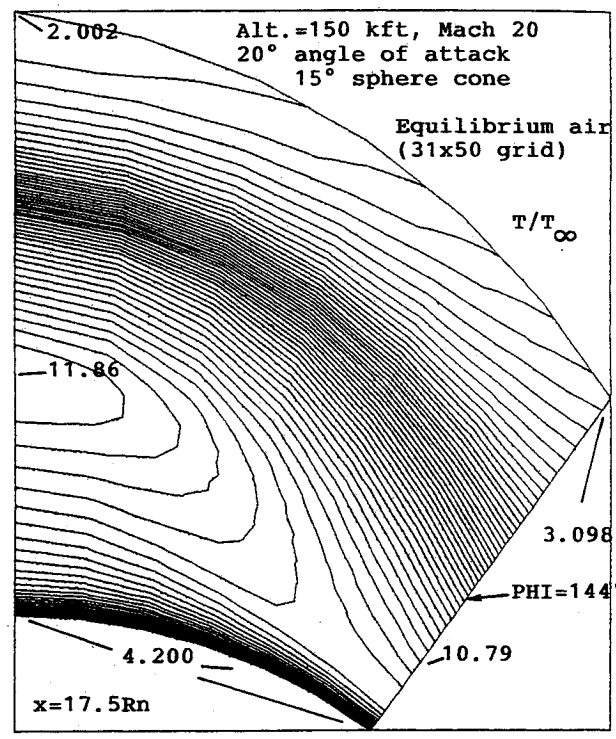

Fig. 7b Details of the lee side temperature contours for case 2b.

mental predictions of the wall heat-transfer rate are also shown in these figures. Figure 5 indicates that the numerical predictions and experimental data are in excellent agreement along the $\phi = 0$ deg and $\phi = 90$ deg planes. The leeward distribution shows a sudden rise in the experimental predictions of wall heat-transfer rate around $x/\mathrm{Rn} = 6$. This rise occurs because the experimental flow on the lee side became transitional around this region.[17] The windward side, however, remained laminar. This can also be seen from the crossflow distribution of Fig. 6. This figure indicates that the numerical predictions are in excellent agreement with the experimental data up to $\phi = 160$ deg. Beyond this point, the experimental data are higher because of transitional flow conditions.

We also did some grid-refinement studies to evaluate the effects of crossflow grid refinement on the accuracy and stability of the solution scheme. Three different grids were used with 31, 25, and 17 equally spaced crossflow planes, respectively. In Fig. 6, we see the effects of this crossflow grid refinement on the wall heat-transfer rate, that whereas the windward side remains almost unaffected, the lee side is quite sensitive to the grid refinement. These results demonstrate that the coarse 17-plane solution does not even predict any crossflow separation. The 25- and 31-plane results, however, clearly show a region of crossflow separation between $\phi = 160$ deg and $\phi = 180$ deg. The extent of the separated region predicted by these two fine grids is also in good agreement. Furthermore, the finest crossflow grid (31-plane) solution signifies that the numerical predictions of the location and magnitude of the minimum wall heat-transfer rate are in very good agreement with the corresponding experimental data.

Effects of Equilibrium-Air Gas Model

The perfect-gas and equilibrium-air calculations for case 2 show that the extent of the predicted crossflow separated region is smaller when the equilibrium-air gas model is used. This can be understood when we consider that the effect of the equilibrium-air gas model is to reduce the shock-layer thickness, and this in turn suppresses the crossflow separation. This is important because the equilibrium-air and perfect-gas comparisons are typically made in terms of either the wall-measurable quantities or, in some cases, the effects on the shock-layer thickness. This may be sufficient under small-angle-of-attack conditions; however, the present results show that, under large-angle-of-attack conditions, the use of an equilibrium-air gas model may even change the flowfield character on the lee side by suppressing or limiting the extent of the crossflow separation.

The effects of the gas chemistry on the lee side temperature contours for these cases are plotted in Fig. 7. The corresponding wall-pressure distributions indicate that, along $\phi = 0$ deg and $\phi = 90$ deg planes, the wall-pressure predictions for perfect-gas and equilibrium-air calculations are within 5% of each other; however, along the $\phi = 180$ deg plane, the equilibrium-air gas model predicts a 15% lower pressure. This is due to the smaller crossflow separated region in the case of the equilibrium-air calculation. The corresponding equilibrium-air VSL calculations show that the VSL and PNS wall-pressure predictions differ by nearly 10%. The VSL results shown were not globally iterated and use a coarse 9-plane crossflow grid.

The crossflow distributions of the wall heat-transfer rate are shown in Fig. 8. In this case, the effect of the equilibrium-air gas model is to increase the wall heat-transfer rate along the $\phi = 0$ deg and $\phi = 90$ deg planes by as much as 15%. The VSL calculations for this case predict 15% higher wall heat transfer than the PNS calculations. The corresponding predictions of the streamwise skin-friction coefficient follow the same trends as the wall heat-transfer predictions. The crossflow distribution of the shock-standoff distance at the body end (Fig. 9) shows that, along the windward pitch plane ($\phi = 0$ deg plane), the effect of the equilibrium-air gas model is to reduce the shock-standoff distance by as much as 85%. Along the $\phi = 90$ deg plane, the equilibrium-air calculations predict a 40% thinner shock whereas, along $\phi = 180$ deg, the predicted shock layer is only 10% thinner than the corre-

sponding perfect-gas calculations. The corresponding equilibrium-air VSL calculations show that VSL and PNS predictions of the bow shock shape are within 10% of each other. Again, it should be noted that the VSL results shown were not globally iterated and, in the absence of available experimental data, were used only to cross-check the qualitative aspects of the equilibrium-air PNS calculations.

In order to test the sensitivity of the wall-measurable quantities to the axis-normal grid refinement, we compared the predictions of the case 2b calculations (with 50 points between the body and the shock) with the corresponding case 2c calculations (with 30 points between the body and shock). The results show that, except for the crossflow separated region, the wall-pressure predictions were typically within 1% of each other. The corresponding streamwise skin-friction and wall heat-transfer predictions were within 10% of each other. In the crossflow separated region, these skin-friction and wall heat-transfer differences were of the order of 15–20%. The corresponding results of the shock-shape predictions indicate that the axis-normal grid refinement had less than 1% effect on the predicted shock-standoff distance.

Computing Times

The computing times for the various calculations performed in this study are shown in Table 2. The present solution scheme involves an implicit inversion algorithm in the crossflow direction. Thus, typically, the computing time increases more rapidly than the corresponding increase in the crossflow grid refinement. Even so, the increase is not that much. For example, compared to case 1c, case 1b shows 4% increase in computing time per grid point. On the other hand, case 1a shows shows only a 14% increase in computing time per grid point. The equilbrium-air (case 2b) computing time shows a 3% increase over the corresponding perfect-gas (case 2a) calculations. In terms of the axis-normal grid-refinement effects, we see that although case 2b calculations represent a 70% increase in the number of grid points between the body and the shock, the required computing time is only 60% more. This occurs because, with the larger number of grid points between the body and the shock, the solution converges faster, and this compensates for some of the increase in the computational effort resulting from the increased number of grid points. When considering these computing times, we

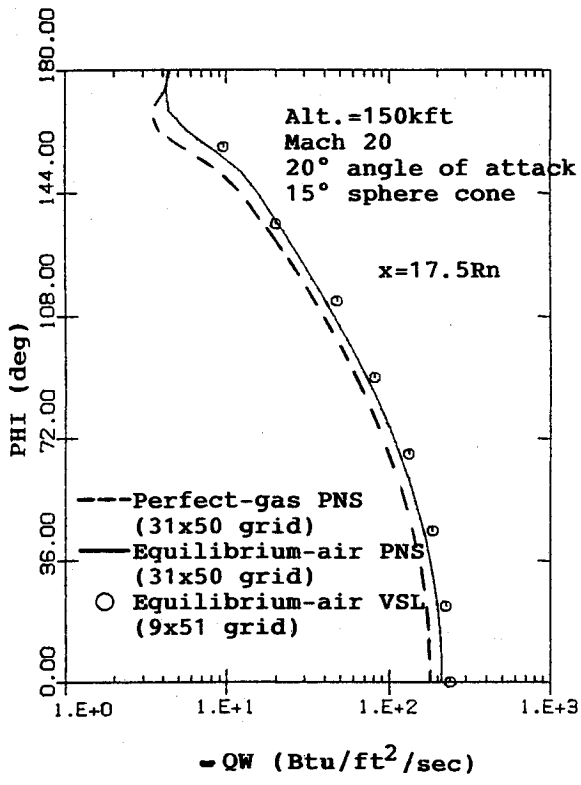

Fig. 8 Effects of gas model on the crossflow distribution of the wall heat-transfer rate for case 2.

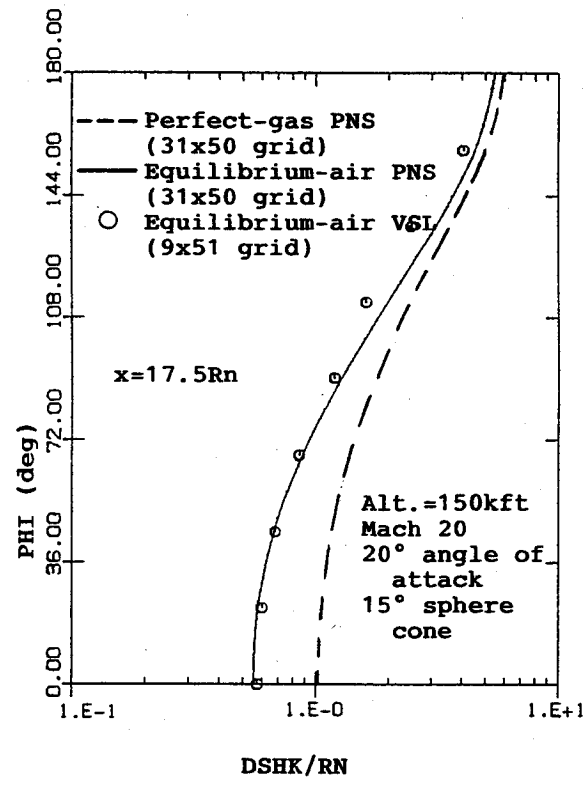

Fig. 9 Effects of gas model on the crossflow variation of the bow shock shape for case 2.

Table 2 Computing times

Case	x/Rn range	Grid $\xi_1 \times \xi_2 \times \xi_3$	IBM3090[a] (min : s)	XMP(4/8)[b] (min : s)	Cray-2[c] (min : s)
Case 1a	1.7–17.5	28 × 50 × 31	4 : 45	1 : 55	3 : 19
Case 1b	1.7–17.5	26 × 50 × 25	3 : 14	1 : 18	2 : 16
Case 1c	1.7–17.5	26 × 50 × 17	2 : 07	0 : 51	1 : 29
Case 2a	3.5–17.5	24 × 50 × 31	6 : 15	2 : 31	4 : 22
Case 2b	3.5–17.5	24 × 50 × 31	6 : 26	2 : 35	4 : 30
Case 2c	3.5–17.5	24 × 30 × 31	4 : 00	1 : 37	2 : 48

[a]Actual computing times on IBM 3090 (model 200VF) with VS-compiler and scalar LEVEL = 3 optimization. [b]Estimated computing times on Cray X-MP (4/8) with CFT77 compiler and auto vectorizaton. [c]Estimated computing times on Cray-2 with CFT77 compiler and auto vectorization.

should also note that the current three-dimensional PNS code is a research code and has not been optimized.

Conclusions

In this study, a new three-dimensional and fully iterative PNS scheme has been developed to study three-dimensional hypersonic flows around ballistic configurations under large angle-of-attack conditions. The flow around a sphere-cone configuration at an angle of attack of 20 deg was considered at two different Mach numbers to study the accuracy and efficiency of this new three-dimensional PNS scheme. Both perfect-gas and equilibrium-air gas models were used. These results substantiate the following conclusions:

1) A new three-dimensional perfect-gas/equilibrium-air PNS scheme has been developed. This scheme is inherently stable in the subsonic as well as the supersonic flow regions and, unlike classical PNS schemes, this new PNS scheme does not require the use of any sublayer approximation. Furthermore, the numerical solution scheme has very good grid-refinement characteristics and permits very fine grids to be used in the near-wall region for improving solution accuracy.

2) The present PNS scheme uses a new simple yet second-order-accurate smoothing approach. The smoothing effects in the axis-normal direction are, however, limited only to the pressure field and, thus, do not degrade the accuracy of the wall heat-transfer and skin-friction predictions.

3) A new predictor-corrector solution scheme has been developed to treat the strong crossflow coupling effects in and around the crossflow separated regions. Furthermore, a new fully implicit shock-prediction scheme has been developed and used to predict accurately the bow shock location as the solution marches down the body. With the use of a pseudo-unsteady algorithm, the present fully iterative three-dimensional results can be accurately and efficiently obtained without any significant computing-time penalty. Furthermore, the enhanced solution accuracy and stability permit the use of much larger marching steps than the noniterative PNS schemes. Thus, the present three-dimensional PNS scheme not only provides more accurate flowfield predictions, but the final computing time required for a typical three-dimensional calculation is generally much shorter than the time required by existing noniterative PNS schemes.

References

[1]Sahu, J. and Nietubicz, C. J., "Improved Numerical Predictions of Transonic Flow," U.S. Army Ballistic Research Laboratory, Aberdeen Proving Ground, MD, BRL-TR-2784, March 1987.

[2]Richardson, P., "High-Speed Configuration Aerodynamic CFD," Paper presented at the First National Aerospace Plane Technology Symposium, Langley Research Center, Hampton, Va, May 1986.

[3]Kumar, A., "High-Speed Inlet Analysis," Paper presented at the First National Aerospace Plane Technology Symposium, Langley Research Center, Hampton, VA, May 1986.

[4]Rizk, Y. M., Chaussee, D. S., and McRae, D. S., "Computations of Hypersonic Viscous Flow Around Three-Dimensional Bodies at High Angle of Attack," AIAA Paper 81-1261, 1981.

[5]Kaul, U. K. and Chaussee, D. S., "AFWAL Parabolized Navier-Stokes Coded: 1983 AFWAL/NASA Merged Baseline Version," Flight Dynamics Laboratory, AF Wright Aeronautical Laboratories, Wright-Patterson AFB, OH, AFWAL-TR-83-3118, Oct. 1983.

[6]Shanks, S. P., Srinivasan, G. R., and Nicolet, W. E., "AFWAL Parabolized Navier-Stokes Code: Formulation and User's-Manual," Air Force Flight Dynamics Laboratory, Wright Patterson AFB, OH, AFWAL-TR-823034, June 1979.

[7]Vigneron, Y. C., Rakich, J. V., and Tannehill, J. C., "Calculations of Supersonic Viscous Flows Over Delta Wings with Sharp Subsonic Leading Edges," AIAA Paper 78-1137, July 1978.

[8]Schiff, L. B. and Steger, J. L., "Numerical Simulation of Steady Supersonic Viscous Flows," AIAA Paper 79-0130, Jan. 1979.

[9]Thareja, R. R., Szema, K. Y., and Lewis, C. H., "Chemical Equilibrium Laminar or Turbulent Three-Dimensional Viscous Shock-Layer Flows," *Journal of Spacecraft and Rockets*, Vol. 20, Sept.–Oct. 1983, pp. 454–460.

[10]Thareja, R. R., Szema, K. Y., and Lewis, C. H., "Viscous Shock-Layer Predictions for Hypersonic Laminar or Turbulent Flows in Chemical Equilibrium Over the Windward Surface of a Shuttle-Like Vehicle," *Progress in Astronautics and Aeronautics*, Vol. 20, No. 5, Sept. 1983, pp. 454–460.

[11]Thompson, R. A., Lewis, C. H., and Kautz, F. A. II, "Comparison Techniques for Predicting 3-D Viscous Flows Over Ablated Shapes," AIAA Paper 8-0345, Jan. 1983.

[12]Bhutta, B. A. and Lewis, C. H., "Low Reynolds Number Flows Past Complex Multiconic Geometries," AIAA Paper 85-0362, Jan. 1985.

[13]Bhutta, B. A. and Lewis, C. H., "An Implicit Parabolized Navier-Stokes Scheme for High-Altitude Reentry Flows," AIAA Paper 85-0036, Jan. 1985.

[14]Bhutta, B. A. and Lewis, C. H., "Prediction of Three-Dimensional Hypersonic Reentry Flows Using a PNS Scheme," *Journal of Spacecraft and Rockets*, Vol. 26, Jan.-Feb. 1989, pp. 4–13.

[15]Bhutta, B. A. and Lewis, C. H., "Parabolized Navier-Stokes Predictions of High-Altitude Re-entry Flowfields," VRA, Inc., Blacksburg, VA, VRA-TR-85-02, April 1985.

[16]Bhutta, B. A., Lewis, C. H., and Kautz, F. A. II, "A Fast Fully-Iterative Parabolized Navier-Stokes Scheme for Chemically-Reacting Reentry Flows," AIAA Paper 85-0926, June 1985.

[17]Cleary, J. W., "Effects of Angle of Attack and Bluntness on Laminar Heating-Rate Distribution of a 15° Cone at a Mach Number of 10.6," NASA TN D-5450, Oct. 1969.

[18]Peyert, R. and Viviand, H., "Computations of Viscous Compressible Flows Based on the Navier-Stokes Equations," AGARD-AG-212, 1975.

[19]Viviand, H., "Conservative Forms of Gas Dynamics Equations," *La Recherche Aérospatiale*, Jan.-Feb. 1974, pp. 65–68.

[20]White, F. M., *Viscous Fluid Flow*, McGraw-Hill, New York, 1974, pp. 28–30.

[21]Miner, E. W., Anderson, E. C., and Lewis, C. H., "A Computer Program for Two-Dimensional and Axisymmetric Nonreacting Perfect Gas and Equilibrium Chemically Reacting Laminar Transitional and/or Turbulent Boundary Layer Flows," Virginia Polytechnic Institute and State University, Blacksburg, VA, VPI-E-71-8, May 1971.

[22]Peng, T. C. and Pindroh, A. L., "An Improved Calculation of Gas Properties at High Temperature Air," Aerospace Division, The Boeing Co., Boeing Rept. D2-11722, 1962.

[23]Murray, A. L. and Lewis, C. H., "Hypersonic Three-Dimensional Viscous Shock-Layer Flows Over Sphere-Cones at High Altitudes and High Angles of Attack," Virginia Polytechnic Institute and State University, Blacksburg, VA, VPI&SU AERO-078, Jan. 1978.

[24]Bhutta, B. A., Kautz, F. A. II, and Lewis, C. H., "Influence of Aerodynamic Prediction Methodology on Performance Evaluation of Reentry Vehicle Configurations," *Journal of Spacecraft and Rockets*, Vol. 22, Sept.-Oct. 1985, pp. 541–547.

[25]Chaussee, D. S., Patterson, J. L., Kutler, P., Pulliam, T. H., and Steger, J. L., "A Numerical Simulation for Hypersonic Viscous Flows Over Arbitrary Geometries at High Angle of Attack," AIAA Paper 81-0050, Jan. 1981.

[26]Helliwell, W. S., Dickinson, R. P., and Lubard, S. C., "Viscous Flows Over Arbitrary Geometries at High Angle of Attack," AIAA Paper 80-0064, Jan. 1980.

[27]Lubard, S. C. and Helliwell, W. S., "Calculation of the Flow on a Cone at High Angle of Attack," R & D Associates, Santa Monica, CA, Rept. RDA-TR-150, Feb. 1973.

[28]Neumann, R. D. and Petterson, J. L., "Results of an Industry Representative Study of Code to Code Validation of Axisymmetric Configurations at Hypervelocity Flight Conditions," AIAA Paper 88-2691, June 1988.